ACCSCIENCE PUBLISHING

International Journal of Bioprinting

RESEARCH ARTICLE

Suspended 3D printing of polycaprolactone/hydroxyapatite composites for the fabrication of complex bone scaffolds

Juhyun Kang[1†], Masoud Shirzad[2†], Priya Ranganathan[2], Dageon Oh[2], Sudip Mondal[3], Junghwan Oh[1,2,4], Hae Gyun Lim[1,2,4], Mahdi Bodaghi[5*], and Seung Yun Nam[1,2,4*]

[1]Department of Biomedical Engineering, Pukyong National University, Busan, Republic of Korea

[2]Industry 4.0 Convergence Bionics Engineering, Pukyong National University, Busan, Republic of Korea

[3]Digital Healthcare Research Center, Institute of Information Technology and Convergence, Pukyong National University, Busan, Republic of Korea

[4]Major of Biomedical Engineering, Division of Smart Healthcare, College of Information Technology and Convergence, Pukyong National University, Busan, Republic of Korea

[5]Department of Engineering, School of Science and Technology, Nottingham Trent University, Nottingham, UK

[†]These authors contributed equally to this work.

***Corresponding authors:**
Seung Yun Nam
(synam@pknu.ac.kr)

Mahdi Bodaghi
(mahdi.bodaghi@ntu.ac.uk)

Citation: Kang J, Shirzad M, Ranganathan P, *et al*. Suspended 3D printing of polycaprolactone/hydroxyapatite composites for the fabrication of complex bone scaffolds. *Int J Bioprint*. 2025;11(6):205-219. doi: 10.36922/IJB025320319

Received: August 8, 2025
1st revised: August 25, 2025
2nd revised: August 29, 2025
Accepted: September 1, 2025
Published Online: September 2, 2025

Abstract

Extrusion-based three-dimensional (3D) printing has been rapidly advancing as a key technique for fabricating tissue-engineering scaffolds. However, printing complex structures with appropriate mechanical strength and biocompatibility remains a challenge. Suspended 3D printing is an emerging fabrication strategy that enables the generation of tissues or organs within a support medium that provides a stable printing environment without the need for additional support structures. This study presents a novel strategy for fabricating intricate scaffolds using suspended 3D printing of bioinks incorporating dissolved polycaprolactone (dPCL) and hydroxyapatite (HA). The optimized dPCL/HA bioink demonstrated up to an 85% reduction in print errors compared to conventional methods, significantly enhancing 3D printability. Moreover, mechanical assessments revealed a compressive Young's modulus approximately 50 MPa higher in dPCL/HA scaffolds compared to dPCL scaffolds. Furthermore, dPCL/HA scaffolds outperformed both PCL and dPCL scaffolds in cell proliferation tests. Complex 3D shapes, including helices, saddles, multi-curvature structures, hollow hemispheres, and zygomatic bones, were successfully fabricated, demonstrating the ability to mimic natural and intricate anatomical structures of the human body. These approaches pave the way for 3D printing patient-specific and structurally robust bone constructs with enhanced mechanical and biological properties.

Keywords: Bone tissue engineering; Biomimetic scaffolds; Composites; Extrusion-based three-dimensional printing; Suspended three-dimensional printing

1. Introduction

Complex bone defects resulting from fractures, osteoporosis, and infections pose significant challenges to the healing process due to the intricate biomechanical and biological demands of bone tissue.[1-3] Addressing these critical requirements necessitates advanced strategies to accelerate healing. The implementation of biocompatible scaffolds represents one such strategy, offering appropriate mechanical and biological properties to support the growth of host tissue.[4] Over the past few years, both conventional and advanced methods have been developed for the fabrication of tissue-engineering scaffolds. Among these methods, extrusion-based three-dimensional (3D) printing has emerged as a promising approach, enabling the construction of scaffolds through the repetitive, layer-by-layer deposition of biomaterials while offering a wide range of material choices.[5–7] However, conventional extrusion-based printing methods face significant limitations, particularly in fabricating complex 3D geometries. These structures often require additional support, making the process time-consuming and less efficient.[8,9]

To overcome these limitations, suspended 3D printing was introduced as an advanced technique, enhancing extrusion-based 3D printing by allowing the fabrication of detailed structures without the need for additional supports.[10-12] This method utilizes a support medium, such as a gel or viscous liquid, to facilitate freeform construction in multiple directions, enabling the creation of complex structures. Moreover, compared with conventional extrusion-based 3D printing, suspended 3D printing offers greater flexibility in material selection, which is particularly advantageous for fabricating functional tissue-engineered constructs.[13–15] This method also promotes the formation of perfusable vascular channels and supports the integration of native tissue components by maintaining the spatial fidelity of soft hydrogels. Despite these advancements, the application of suspended 3D printing in bone tissue engineering remains limited, primarily due to the insufficient mechanical properties of conventional hydrogel-based bioinks, which are often inadequate for load-bearing environments.[16,17] More importantly, most studies employing room-temperature suspended printing have predominantly focused on hydrogel inks rather than thermoplastic polymers.[14,15]

In the fabrication of bone scaffolds, polycaprolactone (PCL) is widely used due to its excellent biocompatibility and favorable mechanical properties. In addition, combining PCL with hydroxyapatite (HA), which constitutes approximately 70% of bone composition, has been extensively investigated, as HA enhances the biofunctionality and compressive modulus of bone scaffolds.[18–22] However, PCL, which is generally printed at 60°C or higher, is unsuitable for suspended printing in gel with high moisture content at room temperature.[23] Notably, one previous study attempted melt-printing of PCL within a thermally stable support matrix. However, this approach required printing at elevated temperatures above 65°C, limiting its applicability under biologically or thermally sensitive conditions.[24]

To address these challenges, this study aims to overcome the limitations associated with conventional 3D printing methods for fabricating complex bone scaffolds by utilizing suspended 3D printing with PCL/HA composites at room temperature. Accordingly, the physicochemical properties of the dissolved PCL (dPCL) integrated with HA were evaluated using Fourier transform infrared spectroscopy (FTIR), X-ray diffraction (XRD), thermogravimetric analysis (TGA), contact angle analysis, scanning electron microscopy (SEM), and field emission SEM (FESEM). Additionally, the printability and rheological properties of the suspended 3D printing process were quantitatively analyzed. The rheological properties were assessed for both the polymer and the composites. Mechanical performance was evaluated under tensile and compressive loads, and cell proliferation was examined using the alamarBlue assay to assess the biological effects of the proposed strategy. A schematic overview of the study design is illustrated in Figure 1. Furthermore, Table 1 provides a comparative summary between the present study and previously published work, highlighting the novelty of this study and demonstrating its advantages over prior studies.

Table 1. Comparison of printing methods for bone scaffold fabrication

Method	Temperature	High viscosity/ mechanical properties	Support printing	Complexity of post-processing	Reference
Suspended	Low	Available	Available	Low	Current study
Suspended	Moderate	N/A	Available	Low	[3,6,10–15,24,40,41,52]
Conventional	High	Variable	N/A	High	[4,5,7,8,20,25,30,34,35,39,42,44,45,49,50,51,53,55–57]
Photo-polymerization	Low	Available	N/A	High	[8,43]

Abbreviation: N/A, not available.

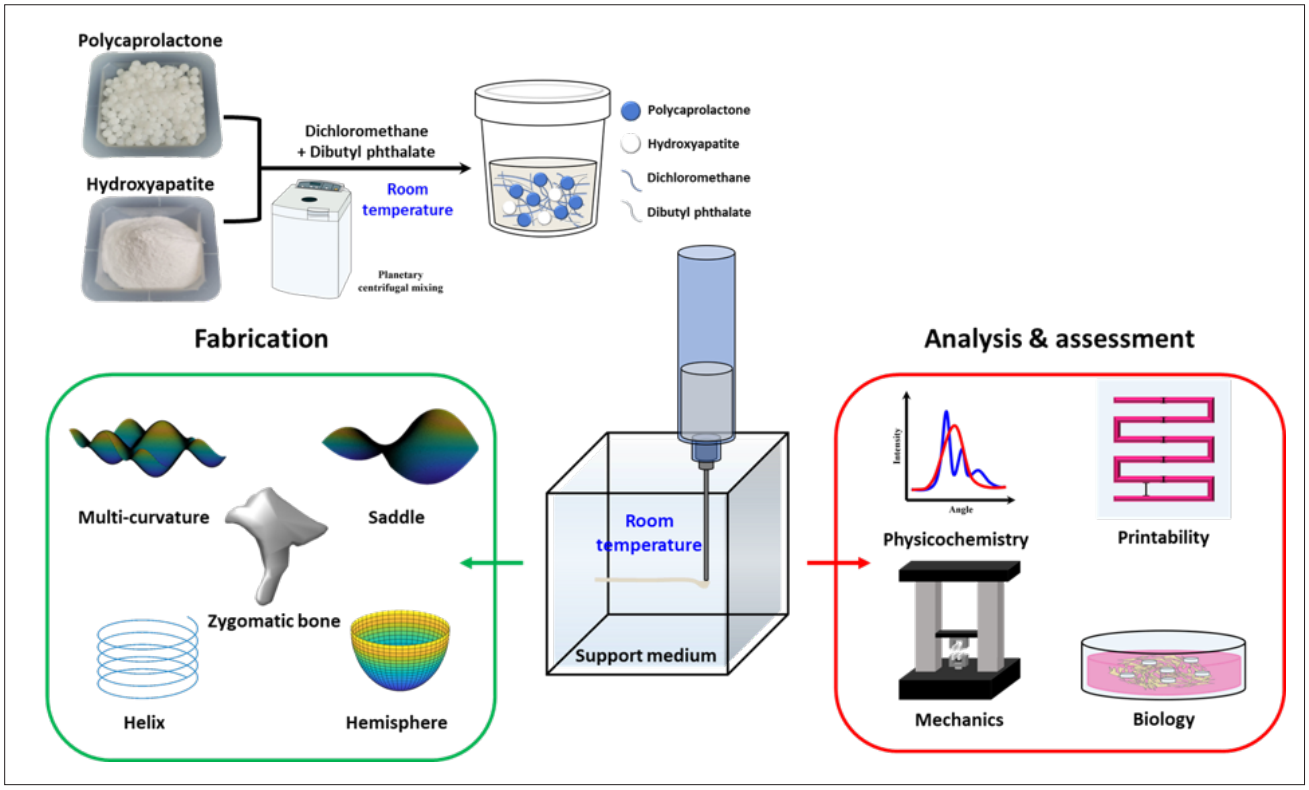

Figure 1. Schematic illustration of the suspended three-dimensional printing process for fabricating complex structures using dissolved polycaprolactone–hydroxyapatite composites.

2. Materials and methods

2.1. Hydroxyapatite synthesis

HA powder was synthesized via a wet precipitation method using calcium nitrate tetrahydrate ($Ca(NO_3)_2{\cdot}4H_2O$; Sigma-Aldrich, USA) and diammonium hydrogen phosphate (Supelco, USA). In this method, ammonium hydroxide solution (28%–30%) (Sigma-Aldrich, USA) was used as the precipitating agent. A 0.24 M solution of $Ca(NO_3)_2{\cdot}4H_2O$ was stirred vigorously at room temperature. Subsequently, a 0.29 M solution of diammonium hydrogen phosphate was slowly added to the $Ca(NO_3)_2{\cdot}4H_2O$ solution. The pH of the final mixture was adjusted to 11 by adding an ammonium hydroxide solution. After a reaction period of 6 hours and an aging period of over 12 hours, the precipitate was filtered from the reaction solution until a neutral pH was reached. The filtered precipitate was dried overnight at 90°C and subsequently calcined at 600°C for one hour in air to remove residual volatiles and ensure crystallinity of the apatite phase prior to compounding.[18]

2.2. Bioink and support medium preparation

A suspended bioink was prepared by dissolving PCL (molecular weight: 50,000; Polysciences, USA) in a binary solvent system consisting of dichloromethane (DCM; Sigma-Aldrich, USA) and dibutyl phthalate (Sigma-Aldrich, USA) mixed at a 10:1 (v/v) ratio relative to the total weight of PCL and HA. This solvent system facilitated extrusion printing at room temperature. The resulting dPCL was combined with HA in a 7:3 (w/w) ratio, yielding a dPCL/HA composite in which HA was uniformly dispersed. Homogenization was achieved using a planetary centrifugal mixer (AR-100, THINKY Corporation, Japan). For comparison, PCL scaffolds were also fabricated by extrusion at 120°C using a customized extrusion-based printer. The Laponite RD-based support medium (BYK, Germany) was prepared at different concentrations by homogeneous mixing with distilled water under magnetic stirring at 500 rpm for 10 minutes. Subsequently, the mixture was transferred to a cubic-shaped container ($40 \times 40 \times 40$ mm^3) and allowed to gel over 24 hours at room temperature.

2.3. Physicochemical analysis

FTIR was conducted using an FTIR instrument (FT-4100, JASCO, Japan) in the scan range of 4000–650 cm^{-1}. XRD analysis (Ultima IV, Rigaku, Japan) was performed using copper Kα radiation (λ = 1.5406 Å) at 40 kV and 30 mA.

The diffraction angles (2θ) were scanned with a step size of 0.02° per second over a range of 10°–70°. The HA powder and fabricated scaffolds were compared with the standard HA diffraction pattern (JCPDS card no. 72-1243). TGA (Discovery TGA 55, TA Instruments, USA) was performed under a nitrogen atmosphere with a heating rate of 10°C/min up to 700°C. Contact angle analysis was performed using a contact angle analyzer (Phoenix-MT, Surface and Electro Optics, South Korea). Morphological analysis was conducted using FESEM operated at 15 kV (MIRA3, Tescan, Czech Republic) and SEM operated at 10 kV (Vega2, Tescan, Czech Republic). Surface roughness (Ra) and structural features were further characterized using a 3D optical profiler (VR-5200, Keyence, Japan), which scans samples vertically on a measurement platform.

2.4. Printability assessment

The rheological properties of the PCL/HA composites were assessed using a rheometer (HR-2, TA Instruments, USA) with a 20 mm parallel plate and a gap of 1000 μm. A solvent trap was used in all assessments to prevent drying. The frequency sweep test of the bioink was performed by varying the angular frequency from 0.1 to 100 rad/s at 25°C with a strain of 0.1%. The recovery test of the support medium involved three steps: the first and third steps were performed at a shear rate of 0.1/s for 60 seconds, and the second step was conducted at a shear rate of 100/s for 10 seconds. All steps were conducted at 25°C.

Additionally, the following printing parameters were used: a pressure of 450 kPa and a 21-gauge (0.52 mm) nozzle. These parameters were applied to assess three factors in two different printing directions: vertical thickness (side), axial position error (side), and horizontal thickness (bottom) at nozzle speeds ranging from 1 to 6 mm/s (Figure 3A).

To measure the thickness of the printed strands, a MATLAB code was implemented to calculate the number of pixels, which was then multiplied by the pixel resolution and converted into millimeters. Any single-line section of the strand that did not match the expected color was excluded to minimize potential errors. Subsequently, the mean and standard deviation values were calculated.

This study focused on the central section to assess the printed strand thickness. The strand step was set to 2 mm for thickness measurement. Thickness was evaluated using **Equation I**:

$$Strand\,thickness\left(mm\right)=\frac{\sum\left(P_N\times P_R\right)}{N} \quad \text{(I)}$$

where P_N is the number of pixels per line, P_R is the pixel resolution (pixels per millimeter), and N is the total number of pixels counted.

Repeated layering was performed after the standard strand with a 2 mm step to assess axial position error. Axial position error was evaluated by using **Equation II**:

$$Axial\,position\,error\left(\%\right)=\frac{H_O-H_D}{H_O}\times 100 \quad \text{(II)}$$

where H_O denotes the original height of the feature, and H_D is the deformed height of the feature.

2.5. Mechanical assessment

The mechanical properties of conventionally printed and suspended 3D-printed scaffolds were evaluated using a universal testing machine (LR5K Plus, LLOYD Instruments, United Kingdom). Compressive specimens were prepared as cubes (5 × 5 × 5 mm^3), and tensile specimens were fabricated as rectangular plates (0.5 × 5 × 30 mm^3). All compression and tensile tests were conducted at a constant crosshead speed.

2.6. Biological analysis

The scaffolds were fabricated as sheets and then punched into discs with a 5 mm biopsy punch. After sterilization with 70% ethanol followed by immersion in phosphate-buffered saline for seven days, the scaffolds were preconditioned in Dulbecco's modified Eagle's medium at 37°C in a humidified atmosphere of 5% CO_2 for 24 hours before cell seeding. Rat adipose-derived mesenchymal stem cells (rADSCs, Cyagen, USA) at passage 5 were seeded onto the scaffolds at a density of 2.0×10^5 cells per scaffold. The cells were then cultured in Dulbecco's modified Eagle's medium supplemented with 10% fetal bovine serum and 1% penicillin–streptomycin at 37°C with 5% CO_2. After one day of cultivation, cell proliferation was determined using alamarBlue reagent (alamarBlue™, Invitrogen, USA) by incubating the scaffolds for four hours with 10% alamarBlue reagent at 37°C. The alamarBlue assay was quantified using a ultraviolet-visible spectrophotometer (Epoch, BioTek, USA) at absorbance wavelengths of 570 nm and 600 nm.

3. Results and discussion

A comprehensive physicochemical analysis was performed to verify the preservation of the chemical and structural properties of PCL and HA, confirming stable synthesis and efficient mixing of the materials. Figure 2A shows the FTIR spectra of the HA, PCL, and PCL-based composites. The synthesized HA exhibited characteristic peaks at 962,

1024, and 1088 cm^{-1}, attributed to P–O bending vibrations, along with a peak at 3573 cm^{-1}, corresponding to O–H stretching from hydroxyl groups. The spectra of PCL and dPCL showed peaks at 1164 and 1238 cm^{-1} for C–O–C, 1721 cm^{-1} for C=O stretching of ester groups, and 2866 and 2942 cm^{-1} for C–H stretching. Notably, the spectra of dPCL closely resembled those of PCL, indicating that dissolution and processing of PCL did not significantly alter its chemical structure. In the dPCL/HA composite, a reduction in transmittance was observed at the C=O and C–H bonds compared with pure PCL and HA. However, the retention of most characteristic peaks from both PCL and HA confirmed that the chemical properties of these materials were preserved during synthesis and mixing. This finding indicates successful integration of HA into PCL without significant chemical degradation.

Figure 2B shows the XRD patterns of PCL, HA, and dPCL/HA, providing insights into their crystalline structures. The dPCL exhibited characteristic peaks at 2θ values of 21.5° and 23.8°, corresponding to the crystalline structures of PCL. These peaks were also prominent in the dPCL/HA composite, indicating that incorporation of HA did not disrupt the crystalline structure of PCL. The HA peaks at 2θ values of 25.87°, 31.74°, and 32.86° corresponded to the reference data (JCPDS card no. 72-1243). In the dPCL/HA composite, weaker HA peaks were observed, suggesting partial crystallization of HA within the composite. Importantly, despite this partial crystallization, the primary crystalline features of PCL were preserved, as confirmed by the consistent peaks.

As illustrated in Figure 2G, TGA analysis was conducted to evaluate the thermal stability of the composite. HA demonstrated high thermal stability up to 700°C. In contrast,

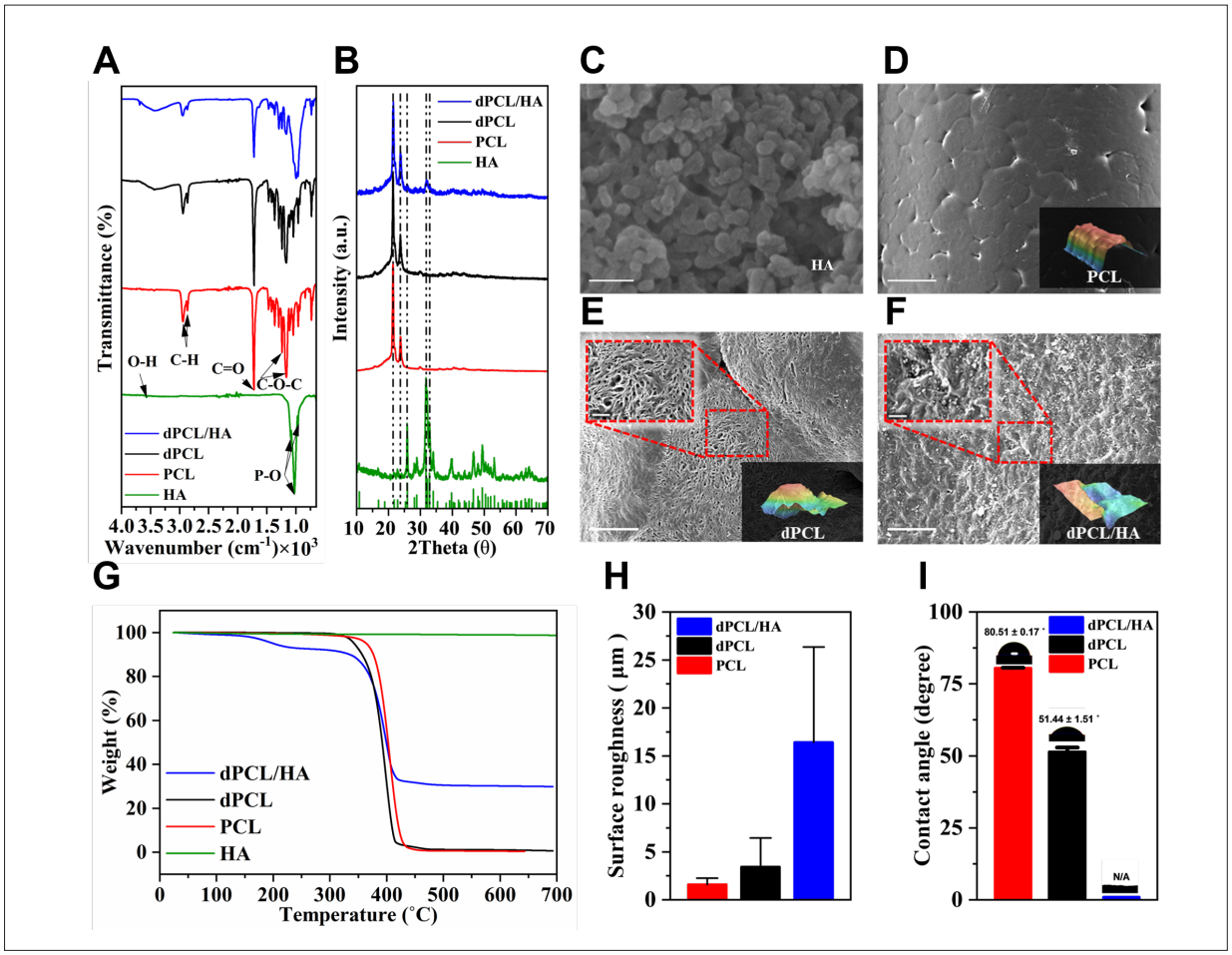

Figure 2. Characterization of PCL, dPCL, HA, and dPCL/HA scaffolds. (A) Fourier transform infrared spectra. (B) X-ray diffraction patterns. (C) Field emission scanning electron microscopy image of HA particles (scale bar: 100 nm; magnification: 400×). (D–F) Scanning electron microscopy images of (D) PCL, (E) dPCL, and (F) dPCL/HA scaffolds (scale bar: 50 μm; magnification: 1×; insets in E and F: 10 μm; magnification: 5×). (G) Thermogravimetric analysis curves. (H) Surface roughness profiles. (I) Contact angle values. Abbreviations: dPCL, dissolved polycaprolactone; HA, hydroxyapatite; N/A, not available; PCL, polycaprolactone.

both dPCL and dPCL/HA exhibited significant weight loss beginning at approximately 400°C, corresponding to the thermal decomposition of PCL. Interestingly, dPCL/HA retained approximately 30% residual mass at elevated temperatures, which was attributed to the incorporation of non-combustible HA within the composite. Furthermore, this value was consistent with the intended 7:3 (w/w) composition, serving as an indirect indicator of batch-level compositional uniformity. Although the thermal degradation rates of both dPCL and dPCL/HA were slightly accelerated compared to pure PCL, the differences remained within acceptable limits, indicating that the composite materials possessed sufficient thermal stability for practical applications. This stability is essential for ensuring reliable material performance in bone tissue engineering applications.

The HA particles were synthesized using the wet method, with a size of approximately 50 nm (Figure 2C). Figure 2D and E shows the SEM images of PCL and dPCL, respectively. Although inter-pore connectivity was not clearly visible, micropores were distributed across the dPCL surface (Figure 2E). Notably, these micropores were not observed in pure PCL, suggesting that solvent evaporation induced surface porosity in dPCL. The microstructures observed in these samples were comparable to the morphological properties of specimens prepared via a gas foaming process.[25] These findings supported the assumption that the microporous structure in dPCL formed as a direct result of DCM volatilization. However, in Figure 2F, dPCL/HA did not exhibit a pattern similar to dPCL, instead displaying irregular topography with HA particles and crater-like features. These findings confirmed that HA could fill the voids created by DCM.

As depicted in Figure 2H, dPCL/HA (16.4 ± 9.9 μm) exhibited significantly higher surface roughness compared to dPCL (3.4 ± 3.0 μm) and PCL (1.6 ± 0.7 μm). This increased surface roughness may provide a more suitable biocompatible environment. Interestingly, a notable difference in contact angle was observed between dPCL (51.44 ± 1.51°) and PCL (80.51 ± 0.17°) (Figure 2I). The contact angle of dPCL/HA could not be accurately determined, as water was fully absorbed at the initial stage of the assessment, possibly due to the vaporization of DCM and the strong hydrophilic properties of HA.[26,27] Consequently, the microporosity induced by DCM in dPCL significantly improved surface roughness and reduced the contact angle, while HA incorporation further enhanced these properties. These modifications are particularly beneficial for enhancing the bioactivity of the composite, as both increased surface roughness and hydrophilicity are strongly correlated with improved cellular attachment and tissue integration.[28] Overall, these findings suggest that the dPCL/HA composite possesses favorable physicochemical and surface properties, making it highly promising for biomaterial applications, particularly in applications requiring enhanced biocompatibility and cell–material interactions. Such enhancements significantly increase the potential of dPCL/HA composites in biomaterial applications.[29,30]

Moreover, the rheological properties of the prepared dPCL and dPCL/HA were assessed using a frequency sweep test. As shown in Figure 3B and C, the PCL-based ink demonstrated highly consistent viscosity. Both the storage modulus (G') and the loss modulus (G") exhibited a consistent, nearly linear increase with angular frequency ranging from 0.1 to 100 rad/s. However, the crossover phenomenon, typically defined as the point where G' and G" intersect in hydrogel-based inks, was not observed.[31,32] The absence of a crossover point indicates that the solid-like viscoelastic behavior of dPCL maintains stable rheological properties even as the frequency increases.[33–35]

The complex viscosity of both dPCL and dPCL/HA inks was consistently maintained at approximately 190 Pa·s across the entire frequency range (0.1–100 rad/s). This stable viscosity facilitated uniform extrusion flow under varying shear conditions, making it particularly suitable for suspended 3D printing. Consequently, PCL-based inks exhibited stable elastic behavior even at elevated frequencies, indicating minimal changes in their network structure. These rheological properties render dPCL and dPCL/HA inks particularly advantageous compared to hydrogel-based inks, which frequently show lower viscosity and reduced structural stability at higher shear rates.[33,36]

The Laponite RD-based support medium provides a stable suspended 3D printing environment for dPCL and dPCL/HA inks. Thixotropic behavior, defined as a reversible decrease in viscosity under applied stress followed by recovery upon stress removal, is a key factor influencing the recovery performance of Laponite RD. This recovery behavior strongly depends on both the strength of the particle network structure and the concentration of Laponite RD (Figure 3D).[37] At concentrations of 3% and 4%, a noticeable gap was observed between the pre- and post-stress viscosities, indicating incomplete recovery due to insufficient network density. In contrast, the 5% and 6% concentrations exhibited nearly identical pre- and post-stress viscosities, reflecting a denser particle network that facilitates faster recovery. However, this rapid recovery can hinder strand formation, as the support medium stabilizes quickly and prevents sufficient spreading of the extruded bioink to fill cracks or voids generated by nozzle movement.[15]

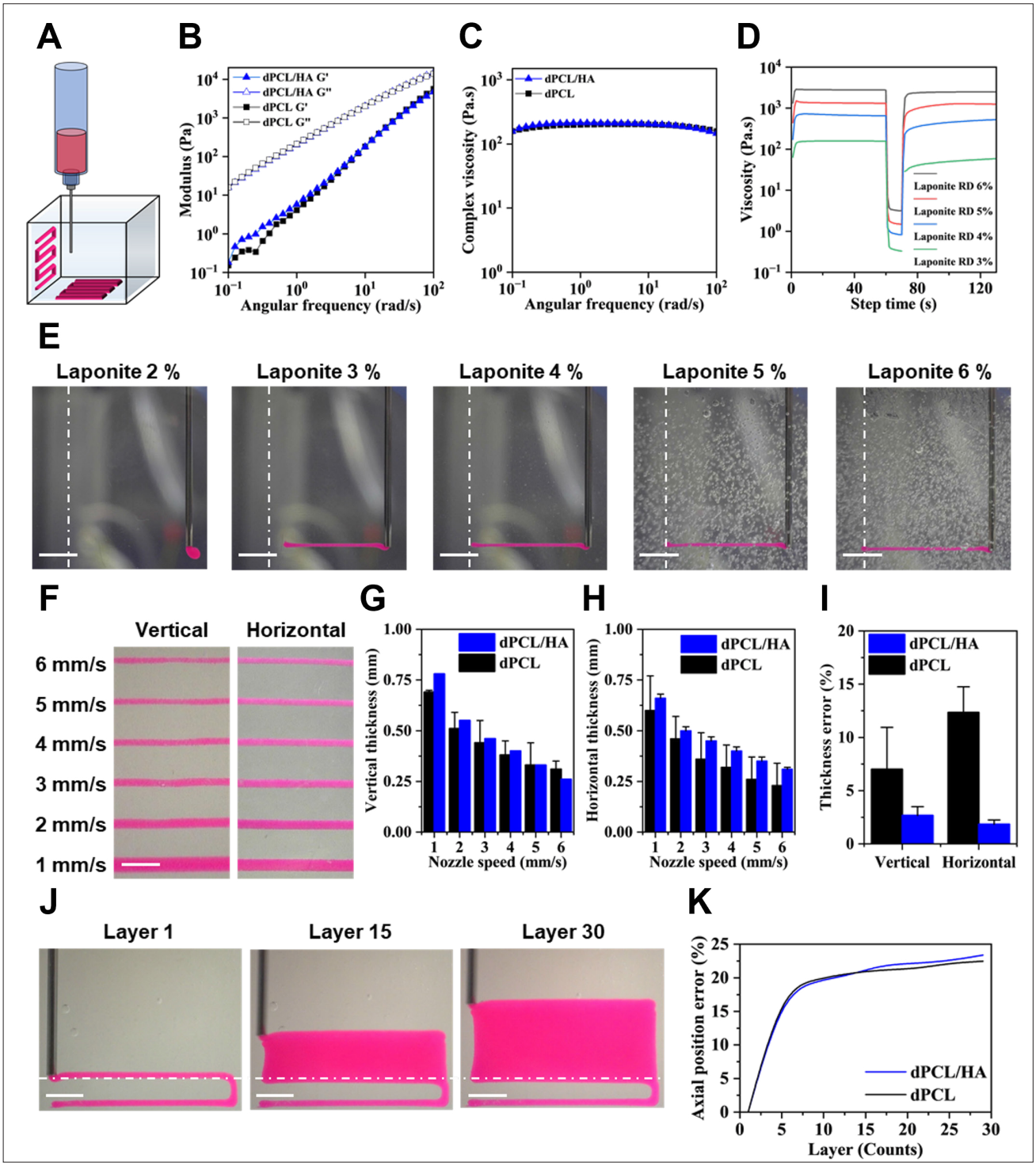

Figure 3. Comprehensive evaluation of rheological properties and print performance of dPCL and dPCL/HA. (A) Schematic illustration of the printability assessment. (B) Storage modulus (G'), loss modulus (G"), and (C) complex viscosity from frequency sweep tests of dPCL and dPCL/HA. (D) Flow peak–hold test of the support media with different concentrations. (E) Printing test of the support media (scale bar: 5 mm). (F) Strand thickness tests at varying nozzle speeds (scale bar: 2 mm). Strand thickness measurements in the (G) vertical and (H) horizontal directions. (I) Strand thickness errors for both vertical and horizontal directions. (J) Images of axial position error tests (scale bar: 2 mm). (K) Numerical evaluation of error rate with increasing layers. Abbreviations: dPCL, dissolved polycaprolactone; HA, hydroxyapatite; PCL, polycaprolactone.

In the next step, the fixation and stability of printed strands were evaluated at various concentrations of the support medium (Figure 3E). The results showed that strands printed in 3%–6% Laponite solutions remained fixed, while the 2% concentration produced unstable shapes, forming irregular bioink bumps rather than defined structures. Although 5% and 6% concentrations provided sufficient fixation, the support medium trapped bubbles and developed crevices during the printing process. These structural instabilities compromised print quality by affecting the medium's uniformity and consistency. Based on these findings, the 4% concentration was identified as the most reliable condition for stable suspended printing.

As shown in Figure 3F, the variation in strand thickness at different nozzle speeds was assessed. At a nozzle speed of 1 mm/s, the strand thickness exceeded the nozzle diameter (21 G, 0.51 mm) in both orientations. However, as nozzle speed increased, strand thickness decreased steadily, ultimately dropping below the nozzle diameter. Among all tested speeds, a nozzle speed of 2 mm/s produced the most consistent and accurate strand thickness, closely matching the nozzle diameter in both vertical (dPCL: 0.51 ± 0.08 mm; dPCL/HA: 0.55 ± 0.02 mm) and horizontal (dPCL: 0.46 ± 0.11 mm; dPCL/HA: 0.50 ± 0.02 mm) orientations (Figure 3G and H). Accordingly, 2 mm/s was determined to be the optimal printing speed for achieving uniform extrusion with minimal thickness deviation.

Subsequently, strand thickness error was assessed in both vertical and horizontal orientations, as shown in Figure 3I. The results revealed that strand thickness errors varied between orientations, with vertical strands showing lower error than horizontal strands, indicating superior control and stability in the vertical direction. Compared to dPCL alone, the dPCL/HA composite showed a 70% enhancement in printability in the vertical direction and an 85% enhancement in the horizontal direction. This improvement is attributed to the presence of HA particles, which act as physical reinforcements within the bioink. These particles contributed to maintaining printed shape fidelity by reducing spreading and deformation following extrusion, thereby increasing consistency in line thickness and improving overall printing accuracy.[23,38,39] This study also investigated axial position error, a key parameter in 3D printing. This improvement effectively reduced thickness errors in both vertical and horizontal orientations. However, the first ten layers exhibited increased deposition errors, with positional error values reaching approximately 20%–25% (Figure 3K). This phenomenon is attributed to the unique environment of suspended 3D printing, where the nozzle is positioned within the support medium.[12,15] During this phase, gaps temporarily form and are subsequently refilled as the support medium recovers. During initial layer deposition, the nozzle displaces the previously recovered support medium surrounding the printed strands, significantly reducing the accuracy of initial deposition.

In contrast to conventional 3D printing methods, suspended 3D printing necessitated a narrower vertical printing step size to achieve stable layering, which contributed to higher positional errors in the initial layers. Beyond the tenth layer, the positional error decreased significantly and stabilized at a value below 1%. This stabilization likely resulted from the support medium and nozzle reaching equilibrium, mitigating the effects of temporary pressure differences.[15,40] Both dPCL and dPCL/HA inks showed nearly identical outcomes, with no significant differences in positional error (Figure 3I). The observed stabilization is crucial for achieving reliable and precise structures in suspended 3D printing, particularly for ensuring consistent accuracy in subsequent layers. These findings underscore the robustness and reliability of the printing process.

Based on these findings, suspended 3D printing offers a significant advantage in fabricating intricate, unsupported geometries that are challenging for conventional extrusion-based methods. As exemplified by the helical structure in Figure 4, this technique enabled the creation of continuous, linear curved forms.[41] However, conventional extrusion techniques inherently struggle to fabricate complex geometries without relying on additional support structures.[42,43] The hemisphere, saddle, and multi-curvature structures further demonstrated the distinct capabilities of suspended 3D printing for fabricating complex geometries without the need for internal infill or support structures. The hemisphere confirmed the feasibility of producing hollow forms in both horizontal and vertical orientations, thereby enhancing material efficiency and reducing processing time. Concurrently, the saddle and multi-curvature structures—defined by continuous topographical variation—expanded the applicability of suspended printing to geometries with higher structural complexity than flat planes.[44,45] This capability to reliably deposit materials on surfaces with varying curvature radii highlights the potential of suspended 3D printing for freeform shape fabrication.

A more advanced and practical structure was fabricated to further demonstrate the feasibility of this method compared to conventional extrusion-based techniques. A natural zygomatic bone was selected for fabrication using the suspended 3D printing method, as its continuous curvature variations and multi-layered configurations pose technical challenges for support-free printing.[46-49] The zygomatic bone is a critical component of the facial

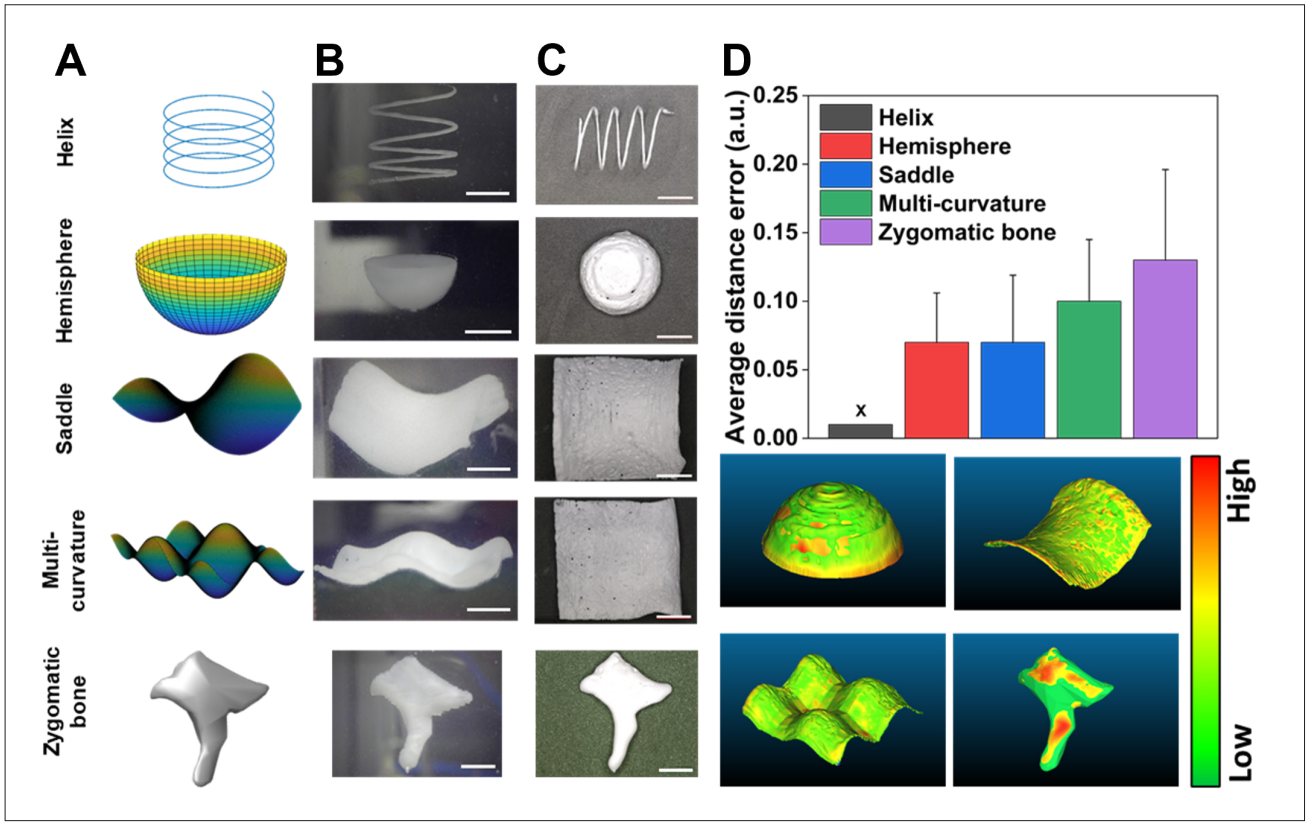

Figure 4. Suspended 3D printing of complex structures, including a helix, saddle, multi-curvature, hemisphere, and zygomatic bone. (A) Structure designs, (B) suspended 3D-printed structures within the support medium (scale bar: 5 mm), (C) structures after removal of the support medium (scale bar: 5 mm), and (D) shape fidelity analysis: average distance error (a.u.) between the reference STL and the scanned printed STL for each geometry, computed in CloudCompare. Abbreviation: 3D, three-dimensional.

skeleton, playing an essential role in maintaining facial structure and protecting the ocular region. However, its complex, curved surface architecture renders it particularly vulnerable to deformation caused by gravity when fabricated using conventional extrusion-based 3D printing techniques.[47,49,50]

As shown in Figure 4D, structural comparisons were performed using a 3D optical profiler. The printed zygomatic bone was vertically scanned, and deviations from the reference model were subsequently analyzed. The geometric discrepancies were quantified using CloudCompare software (Telecom Paris Tech and EDF R&D, France) and represented through a color map, with red indicating larger deviations and green representing smaller errors. The findings confirmed consistent printing precision across a wide range of geometries, with minimal substantial deviations. A comparative analysis between the designed STL format model and the scanned suspended structure revealed that increasing geometric complexity led to a gradual increase in average distance error, reaching over 0.1 mm.[51,52] As shown in Figure 5, the structures fabricated using the suspended 3D printing method exhibited superior and more consistent print quality in all four directions (front, back, left, and right) compared to those produced by conventional fused deposition modeling techniques.[8,9,53]

In this study, the mechanical and biological properties of the scaffolds were experimentally investigated. As depicted in Figure 6B–E, the compressive moduli were measured for dPCL/HA (105.06 ± 24.87 MPa), dPCL (58.22 ± 0.73 MPa), and PCL (136.83 ± 22.37 MPa). Among all materials, dPCL had the lowest compressive modulus, possibly due to its morphology, as observed in the structural analysis, which showed higher porosity, potentially leading to a reduction in mechanical properties (see Figure 2C–F). The compressive stress–strain curve of dPCL/HA exhibited a significant increase after 20% strain, reflecting enhanced resistance to deformation under compressive loads. Additionally, dPCL showed a steady increase in stress but with lower compressive strength compared to dPCL/HA. The enhancement in compressive modulus is attributed to the conversion of porous regions

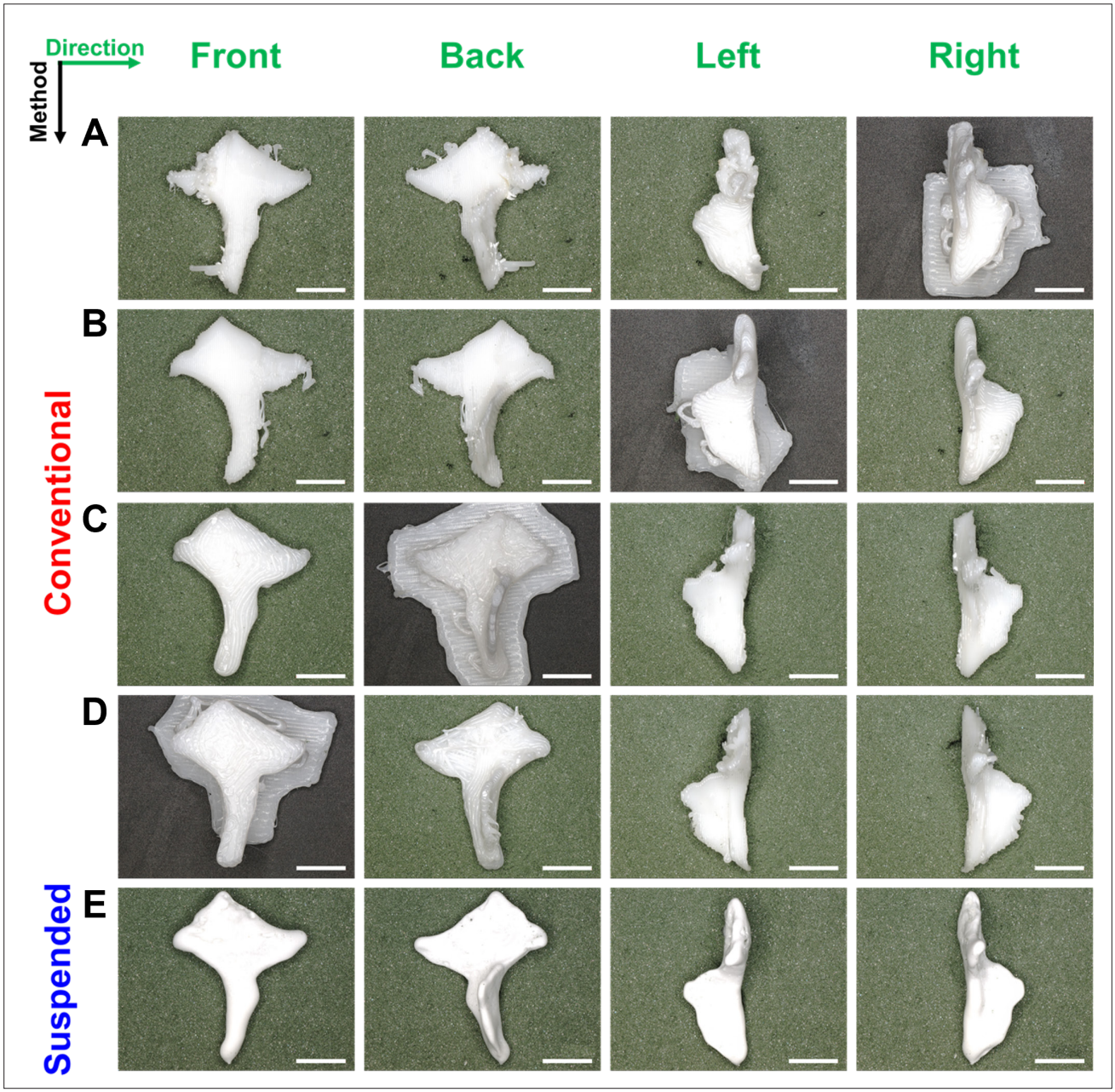

Figure 5. Comparison of zygomatic bone structures fabricated using suspended and conventional extrusion-based three-dimensional printing. (A–D) Structures printed using the conventional method in the (A) rightward, (B) leftward, (C) backward, and (D) forward directions. (E) Structures fabricated using suspended three-dimensional printing, shown from the front, back, left, and right views (scale bar: 5 mm).

within the scaffold into denser, non-porous structures. The generation of microscale voids during solvent evaporation was found to compromise the structural integrity of the material. While dPCL exhibited superior tensile strength, its compressive strength was reduced due to the presence of voids. Conversely, in the dPCL/HA composite, HA particles embedded within the dPCL matrix served as structural reinforcements, effectively compensating for this limitation. This enhanced mechanical support suggests that dPCL/HA is more suitable than dPCL alone for load-bearing bone applications.[26] Consequently, the addition of HA enhanced the compressive properties, consistent with previous studies highlighting the beneficial effects of HA in composite materials.[20,22,54]

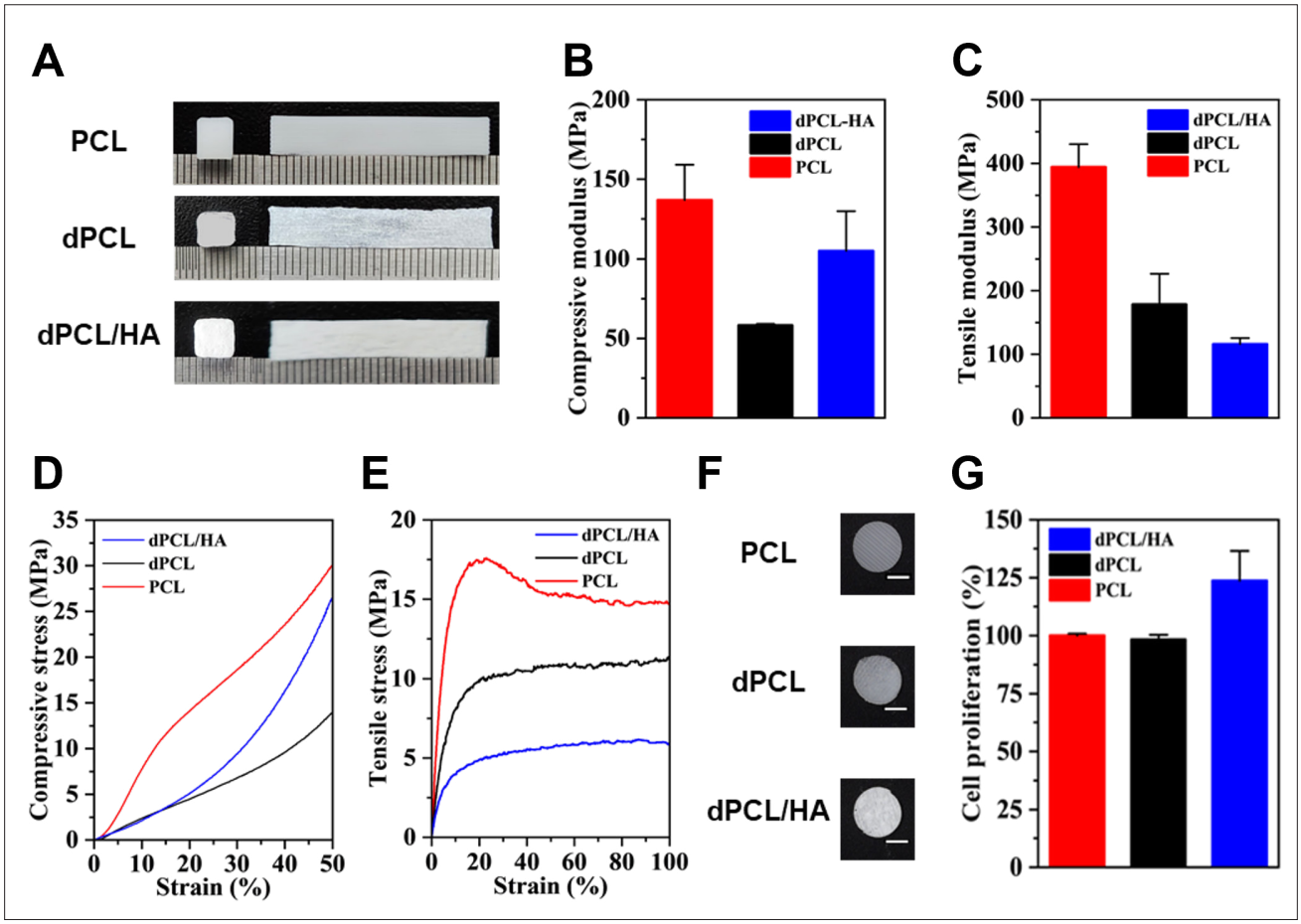

Figure 6. Mechanical and biological properties of PCL, dPCL, and dPCL/HA scaffolds. (A) Fabricated specimens used for mechanical assessment. (B) Compressive modulus and (C) tensile modulus of PCL, dPCL, and dPCL/HA. (D) Compressive modulus and (E) tensile stress–strain curves. (F) Specimens used for biological analysis (scale bar: 2 mm). (G) Cell proliferation of rat adipose-derived mesenchymal stem cells on various scaffolds. Abbreviations: dPCL, dissolved polycaprolactone; HA, hydroxyapatite; PCL, polycaprolactone.

In the tensile test, the results revealed the tensile moduli for dPCL/HA (116.10 ± 9.39 MPa), dPCL (178.37 ± 47.86 MPa), and PCL (394.05 ± 36.35 MPa). Contrary to the compressive test, dPCL showed a higher tensile modulus than dPCL/HA. All three bioinks exhibited a significant increase in stress up to 20% strain; however, their trends diverged thereafter depending on the material composition. For PCL, stress decreased after 20% strain until approximately 50%, after which it stabilized. In contrast, both dPCL/HA and dPCL maintained relatively stable stress profiles beyond 20% strain. Furthermore, dPCL/HA and dPCL demonstrated lower tensile performance overall, with dPCL/HA exhibiting even lower values than dPCL. This reduction is attributed to the presence of HA interfering with the intermolecular bonding of PCL, consistent with previous studies.[1,54] Notably, the mechanical properties of dPCL/HA fall within the range of tensile properties of cancellous bone, suggesting its potential suitability for applications in load-bearing bone scaffolds.[55,56]

The cell proliferation of rADSCs on both PCL and PCL-based composite scaffolds was assessed using the alamarBlue assay (Figure 6G). The results showed comparable cell proliferation for PCL (100%) and dPCL (98.28%), while dPCL/HA (123.72%) exhibited higher cell proliferation than both control (PCL) and dPCL. The comparative analysis yielded equivalent biocompatibility for rADSCs cultured on both PCL and dPCL scaffolds, implying that dPCL did not adversely affect cellular viability after fabrication. However, no significant difference in cell proliferation was observed between PCL and dPCL, despite their morphological differences.[30,57] In contrast, dPCL/HA demonstrated a marked improvement in cell proliferation, surpassing that of both PCL and dPCL. This enhancement suggests a pivotal role for HA

in promoting biocompatibility, supported by both the morphological characteristics observed in this study and previous findings.[26] These results highlight the potential of dPCL/HA scaffolds for improved cell compatibility in bone tissue engineering applications.

4. Conclusion

In conclusion, dPCL/HA scaffolds were systematically evaluated using suspended 3D printing to assess both material and structural performance. To fabricate precisely controlled scaffolds, a comprehensive printability assessment was conducted to optimize the key printing parameters. The incorporation of HA into dPCL significantly enhanced printability, improving resolution by up to 85% in the horizontal direction compared to pure dPCL. This advancement enabled the fabrication of complex geometries without the need for additional support structures. In addition, the dPCL/HA scaffolds showed improved mechanical performance, with compressive strengths approximately 50 MPa higher than dPCL alone. In contrast to conventional printing methods, the proposed support-free suspended printing strategy demonstrated the capability to produce structurally intricate constructs. These findings suggest that the developed room-temperature, dPCL-based suspended printing approach holds significant promise for fabricating geometrically complex and biocompatible scaffolds in bone tissue engineering applications.

Acknowledgments

None.

Funding

This research was supported by a National Research Foundation of Korea grant (NRF-2021R1I1A3040459) funded by the Ministry of Education, Republic of Korea, and by a Korea Health Technology R&D Project grant through the Korea Health Industry Development Institute, funded by the Ministry of Health and Welfare, Republic of Korea (HI22C1323).

Conflict of interest

Seung Yun Nam serves as the Editorial Board Member of the journal, but did not in any way involve in the editorial and peer-review process conducted for this paper, directly or indirectly. Other authors declare they have no competing interests.

Author contributions

Conceptualization: Juhyun Kang, Masoud Shirzad, Seung Yun Nam
Data curation: Juhyun Kang, Masoud Shirzad
Formal analysis: Juhyun Kang
Funding acquisition: Seung Yun Nam
Investigation: Juhyun Kang, Masoud Shirzad, Mahdi Bodaghi, Sudip Mondal, Hae Gyun Lim, Junghwan Oh
Methodology: Juhyun Kang, Masoud Shirzad, Priya Ranganathan, Dageon Oh, Sudip Mondal
Project administration: Seung Yun Nam
Resource: Seung Yun Nam
Software: Juhyun Kang
Supervision: Seung Yun Nam
Validation: Juhyun Kang
Visualization: Juhyun Kang, Masoud Shirzad
Writing–original draft: Juhyun Kang, Masoud Shirzad
Writing–review & editing: All authors

Ethics approval and consent to participate

Not applicable.

Consent for publication

Not applicable.

Availability of data

The data that support the findings of this study are available from the corresponding author upon reasonable request.

References

1. Deng X, Yu C, Zhang X, *et al*. A chitosan-coated PCL/nano-hydroxyapatite aerogel integrated with a nanofiber membrane for providing antibacterial activity and guiding bone regeneration. *Nanoscale*. 2024;16(20):9861-9874. doi: 10.1039/d4nr00563e
2. Song T, Zhou J, Shi M, *et al*. Osteon-mimetic 3D nanofibrous scaffold enhances stem cell proliferation and osteogenic differentiation for bone regeneration. *Biomater Sci*. 2022;10(4):1090-1103. doi: 10.1039/d1bm01489g
3. Romanazzo S, Hudson AR, Shiwarski DJ, *et al*. Synthetic bone-like structures through omnidirectional ceramic bioprinting in cell suspensions. *Adv Funct Mater*. 2021;31(13):2008216. doi: 10.1002/adfm.202008216
4. Kim MH, Chalisserry EP, Mondal S, Oh J, Nam SY. Silicon-substituted hydroxyapatite reinforced 3D printed gelatin membrane for guided bone regeneration. *Mater Lett*. 2021;304:130670. doi: 10.1016/j.matlet.2021.130670
5. Lee H, Yoo JM, Ponnusamy NK, Nam SY. 3D-printed hydroxyapatite/gelatin bone scaffolds reinforced with graphene oxide: optimized fabrication and mechanical characterization. *Ceram Int*. 2022;48(7):10155-10163. doi: 10.1016/j.ceramint.2021.12.227

6. Montalbano G, Molino G, Fiorilli S, Vitale-Brovarone C. Synthesis and incorporation of rod-like nano-hydroxyapatite into type I collagen matrix: a hybrid formulation for 3D printing of bone scaffolds. *J Eur Ceram Soc*. 2020;40(11):3689-3697.
doi: 10.1016/j.jeurceramsoc.2020.02.018

7. Shirzad M, Kang J, Kim G, Bodaghi M, Nam SY. Bioinspired 3D-printed auxetic structures with enhanced fatigue behavior. *Adv Eng Mater*. 2024;26(20):2302036.
doi: 10.1002/adem.202302036

8. Hu K, Jin S, Wang CC. Support slimming for single material based additive manufacturing. *Comput Aided Des*. 2015;65:1-10.
doi: 10.1016/j.cad.2015.03.001

9. Jiang J, Xu X, Stringer J. Support structures for additive manufacturing: a review. *J Manuf Mater Process*. 2018;2(4):64.
doi: 10.3390/jmmp2040064

10. Alioglu MA, Yilmaz YO, Singh YP, *et al*. Nested biofabrication: matryoshka-inspired intra-embedded bioprinting. *Small Methods*. 2023;8(8):e2301325.
doi: 10.1002/smtd.202301325

11. Song KH, Highley CB, Rouff A, Burdick JA. Complex 3D-printed microchannels within cell-degradable hydrogels. *Adv Funct Mater*. 2018;28(31).
doi: 10.1002/adfm.201801331

12. Bhattacharjee T, Zehnder SM, Rowe KG, *et al*. Writing in the granular gel medium. *Sci Adv*. 2015;1(8):e1500655.
doi: 10.1126/sciadv.1500655

13. Wu W, DeConinck A, Lewis JA. Omnidirectional printing of 3D microvascular networks. *Adv Mater*. 2011;23(24):H178-H183.
doi: 10.1002/adma.201004625

14. Jin Y, Compaan A, Chai W, Huang Y. Functional nanoclay suspension for printing-then-solidification of liquid materials. *ACS Appl Mater Interfaces*. 2017;9(23):20057-20066.
doi: 10.1021/acsami.7b02398

15. Lee A, Hudson A, Shiwarski D, *et al*. 3D bioprinting of collagen to rebuild components of the human heart. *Science*. 2019;365(6452):482-487.
doi: 10.1126/science.aav9051

16. Gao C, Sow WT, Wang Y, *et al*. Hydrogel composite scaffolds with an attenuated immunogenicity component for bone tissue engineering applications. *J Mater Chem B*. 2021;9(8):2033-2041.
doi: 10.1039/d0tb02588g

17. Liu L, Yang B, Wang LQ, *et al*. Biomimetic bone tissue engineering hydrogel scaffolds constructed using ordered CNTs and HA induce the proliferation and differentiation of BMSCs. *J Mater Chem B*. 2020;8(3):558-567.
doi: 10.1039/c9tb01804b

18. Mondal S, Dey A, Pal U. Low temperature wet-chemical synthesis of spherical hydroxyapatite nanoparticles and their in situ cytotoxicity study. *Adv Nano Res*. 2016;4(4):295-307.
doi: 10.12989/anr.2016.4.4.295

19. Shi Y, Wang L, Sun L, *et al*. Melt electrospinning writing PCL scaffolds after alkaline modification with outstanding cytocompatibility and osteoinduction. *Int J Bioprint*. 2023;9(6):1071.
doi: 10.36922/ijb.1071

20. Biscaia S, Branquinho MV, Alvites RD, *et al*. 3D printed poly(ε-caprolactone)/hydroxyapatite scaffolds for bone tissue engineering: a comparative study on a composite preparation by melt blending or solvent casting techniques and the influence of bioceramic content on scaffold properties. *Int J Mol Sci*. 2022;23(4):2318.
doi: 10.3390/ijms23042318

21. Rezaei A, Mohammadi MR. Development of hydroxyapatite nanorods-polycaprolactone composites and scaffolds derived from a novel in-situ sol-gel process. *Tissue Eng Regen Med*. 2012;9(6):295-303.
doi: 10.1007/s13770-012-0002-z

22. Wang Y, Liu L, Guo S. Characterization of biodegradable and cytocompatible nano-hydroxyapatite/polycaprolactone porous scaffolds in degradation in vitro. *Polym Degrad Stabil*. 2010;95(2):207-213.
doi: 10.1016/j.polymdegradstab.2009.11.023

23. Cestari F, Petretta M, Yang Y, Motta A, Grigolo B, Sglavo VM. 3D printing of PCL/nano-hydroxyapatite scaffolds derived from biogenic sources for bone tissue engineering. *Sustain Mater Technol*. 2021;29:e00318.
doi: 10.1016/j.susmat.2021.e00318

24. Zeng X, Meng Z, Qiu Z, He J, Fan J, Li D. Melt-based embedded printing for freeform fabrication of overhanging and flexible polycaprolactone scaffolds. *Virt Phys Prototyp*. 2023;18(1).
doi: 10.1080/17452759.2023.2209778

25. Jakus AE, Rutz AL, Jordan SW, *et al*. Hyperelastic "bone": a highly versatile, growth factor-free, osteoregenerative, scalable, and surgically friendly biomaterial. *Sci Transl Med*. 2016;8(358):358ra127.
doi: 10.1126/scitranslmed.aaf7704

26. Moghadam MZ, Hassanajili S, Esmaeilzadeh F, Ayatollahi M, Ahmadi M. Formation of porous HPCL/LPCL/HA scaffolds with supercritical CO2 gas foaming method. *J Mech Behav Biomed Mater*. 2017;69:115-127.
doi: 10.1016/j.jmbbm.2016.12.014

27. Lee H-U, Jeong Y-S, Jeong S-Y, *et al*. Role of reactive gas in atmospheric plasma for cell attachment and proliferation on biocompatible poly ε-caprolactone film. *Appl Surf Sci*. 2008;254(18):5700-5705.
doi: 10.1016/j.apsusc.2008.03.049

28. Liu Z, Liu X, Ramakrishna S. Surface engineering of biomaterials in orthopedic and dental implants: strategies to improve osteointegration, bacteriostatic and bactericidal activities. *Biotechnol J*. 2021;16(7):2000116. doi: 10.1002/biot.20200011

29. Wang L, Wang C, Zhou L, *et al*. Fabrication of a novel three-dimensional porous PCL/PLA tissue engineering scaffold with high connectivity for endothelial cell migration. *Eur Polym J*. 2021;161:110834. doi: 10.1016/j.eurpolymj.2021.110834

30. Ma J, Lin L, Zuo Y, *et al*. Modification of 3D printed PCL scaffolds by PVAc and HA to enhance cytocompatibility and osteogenesis. *RSC Adv*. 2019;9(10):5338-5346. doi: 10.1039/c8ra06652c

31. Oh D, Shirzad M, Kim MC, Chung E-J, Nam SY. Rheology-informed hierarchical machine learning model for the prediction of printing resolution in extrusion-based bioprinting. *Int J Bioprint*. 2023;9(6):1280. doi: 10.36922/ijb.1280

32. Kim MH, Lee YW, Jung WK, Oh J, Nam SY. Enhanced rheological behaviors of alginate hydrogels with carrageenan for extrusion-based bioprinting. *J Mech Behav Biomed Mater*. 2019;98:187-194. doi: 10.1016/j.jmbbm.2019.06.014

33. Huang B, Bártolo PJ. Rheological characterization of polymer/ceramic blends for 3D printing of bone scaffolds. *Polym Test*. 2018;68:365-378. doi: 10.1016/j.polymertesting.2018.04.033

34. He M, Zhang F, Li C, *et al*. Mechanical properties and oral restoration applications of 3D printed aliphatic polyester-calcium composite materials. *Alex Eng J*. 2024;88:245-252. doi: 10.1016/j.aej.2024.01.042

35. Motloung MP, Mofokeng TG, Ray SS. Viscoelastic, thermal, and mechanical properties of melt-processed poly (epsilon-caprolactone) (PCL)/hydroxyapatite (HAP) composites. *Materials (Basel)*. 2021;15(1):104. doi: 10.3390/ma15010104

36. Daskalakis E, Hassan MH, Omar AM, Cooper G, Weightman A, Bartolo P. Rheological behaviour of different composite materials for additive manufacturing of 3D bone scaffolds. *J Mater Res Technol*. 2023;24:3670-3682. doi: 10.1016/j.jmrt.2023.03.231

37. Waters R, Alam P, Pacelli S, Chakravarti AR, Ahmed RP, Paul A. Stem cell-inspired secretome-rich injectable hydrogel to repair injured cardiac tissue. *Acta Biomater*. 2018;69:95-106. doi: 10.1016/j.actbio.2017.12.025

38. Guo C, Wu J, Zeng Y, Li H. Construction of 3D bioprinting of HAP/collagen scaffold in gelation bath for bone tissue engineering. *Regen Biomater*. 2023;10:rbad067. doi: 10.1093/rb/rbad067

39. Milazzo M, Fitzpatrick V, Owens CE, *et al*. 3D printability of silk/hydroxyapatite composites for microprosthetic applications. *ACS Biomater Sci Eng*. 2023;9(3):1285-1295. doi: 10.1021/acsbiomaterials.2c01357

40. Hinton TJ, Jallerat Q, Palchesko RN, *et al*. Three-dimensional printing of complex biological structures by freeform reversible embedding of suspended hydrogels. *Sci Adv*. 2015;1(9):e1500758. doi: 10.1126/sciadv.1500758

41. Wu Q, Zhu F, Wu Z, *et al*. Suspension printing of liquid metal in yield-stress fluid for resilient 3D constructs with electromagnetic functions. *NPJ Flex Electron*. 2022;6(1):50. doi: 10.1038/s41528-022-00184-6

42. Enea S, Moon SK. Guidelines for 3D printed springs using material extrusion. *Rapid Prototyp J*. 2022;28(3):409-427. doi: 10.1108/RPJ-04-2020-0078

43. Okutani C, Yokota T, Miyazako H, Someya T. 3D printed spring-type electronics with liquid metals for highly stretchable conductors and inductive strain/pressure sensors. *Adv Mater Technol*. 2022;7(7):2101657. doi: 10.1002/admt.202101657

44. Rodriguez-Padilla C, Cuan-Urquizo E, Roman-Flores A, Gordillo JL, Vázquez-Hurtado C. Algorithm for the conformal 3D printing on non-planar tessellated surfaces: applicability in patterns and lattices. *Appl Sci*. 2021;11(16):7509. doi: 10.3390/app11167509

45. Abdullah AM, Dunn ML, Yu K. Robotic 3D printing of continuous fiber reinforced thermoset composites. *Adv Mater Technol*. 2024;9(24):2400839. doi: 10.1002/admt.202400839

46. Murali A, Parameswaran R. Extrusion 3D printing advances for craniomaxillofacial bone tissue engineering. *Polym Plast Technol Mater*. 2024;63(7):889-912. doi: 10.1080/25740881.2024.2307351

47. Tao O, Kort-Mascort J, Lin Y, *et al*. The applications of 3D printing for craniofacial tissue engineering. *Micromachines*. 2019;10(7):480. doi: 10.3390/mi10070480

48. Meglioli M, Naveau A, Macaluso GM, Catros S. 3D printed bone models in oral and cranio-maxillofacial surgery: a systematic review. *3D Print Med*. 2020;6(1):30. doi: 10.1186/s41205-020-00082-5.

49. Nyberg E, O'Sullivan A, Grayson W. scafSLICR: a MATLAB-based slicing algorithm to enable 3D-printing of tissue engineering scaffolds with heterogeneous porous microarchitecture. *PLoS One*. 2019;14(11):e0225007. doi: 10.1371/journal.pone.0225007

50. Moiduddin K, Mian SH, Umer U, Alkhalefah H, Ahmed F, Hashmi FH. Design, analysis, and 3D printing of a patient-specific polyetheretherketone implant for the reconstruction of zygomatic deformities. *Polymers*. 2023;15(4):886. doi: 10.3390/polym15040886

51. Van Belleghem S, Torres Jr L, Santoro M, *et al*. Hybrid 3D printing of synthetic and cell-laden bioinks for shape retaining soft tissue grafts. *Adv Funct Mater*. 2020;30(3):1907145.
doi: 10.1002/adfm.201907145

52. Shiwarski DJ, Hudson AR, Tashman JW, *et al*. 3D bioprinting of collagen-based high-resolution internally perfusable scaffolds for engineering fully biologic tissue systems. *Sci Adv*. 2025;11(17):eadu5905.
doi: 10.1126/sciadv.adu5905

53. Guerrero-de-Mier A, Espinosa M, Domínguez M. Bricking: a new slicing method to reduce warping. *Proc Eng*. 2015;132:126-131.
doi: 10.1016/j.proeng.2015.12.488

54. Moeini S, Mohammadi MR, Simchi A. In-situ solvothermal processing of polycaprolactone/hydroxyapatite nanocomposites with enhanced mechanical and biological performance for bone tissue engineering. *Bioact Mater*. 2017;2(3):146-155.
doi: 10.1016/j.bioactmat.2017.04.004

55. Shirzad M, Bodaghi M, Oh D, Yi M, Nam SY. Design and optimization of bioinspired auxetic structure for biomedical applications. *Eur J Mech A Solids*. 2024;103:105139.
doi: 10.1016/j.euromechsol.2023.105139

56. Almela T, Brook IM, Khoshroo K, *et al*. Simulation of cortico-cancellous bone structure by 3D printing of bilayer calcium phosphate-based scaffolds. *Bioprinting*. 2017;6:1-7.
doi: 10.1016/j.bprint.2017.04.001

57. Huang B, Caetano G, Vyas C, Blaker JJ, Diver C, Bartolo P. Polymer-ceramic composite scaffolds: the effect of hydroxyapatite and beta-tri-calcium phosphate. *Materials (Basel)*. 2018;11(1):129.
doi: 10.3390/ma11010129